Materials Science-Poland, 40(1), 2022, pp. 130-144
http://www.materialsscience.pwr.wroc.pl/
DOI: 10.2478/msp-2022-0016

Damage to inverse hybrid laminate structures: an analysis of shear strength test

Mariusz Frankiewicz[1,*], Grzegorz Ziółkowski[1], Robert Dziedzic[1], Tomasz Osiecki[2], Peter Scholz[3]

[1]Centre for Advanced Manufacturing Technologies – Fraunhofer Project Center, Department of Laser Technologies, Automation and Production Management, Faculty of Mechanical Engineering, Wroclaw University of Science andTechnology, Lukasiewicza 5, 50-371 Wroclaw, Poland

[2]Institute of Lightweight Structures and Polymer Technology, Technische Universität Chemnitz, Reichenhainer Str. 31-33, 09126 Chemnitz, Germany

[3]Fraunhofer Institute for Machine Tools and Forming Technology IWU, Reichenhainer Str. 88, 09126 Chemnitz, Germany

Hybrid laminates with continuous fiber reinforcement, such as glass reinforced aluminium laminate (GLARE), aramid reinforced aluminum laminate (ARALL), or carbon reinforced aluminum laminate (CARALL), have been developed to increase the lightweight potential and fatigue resistance applied for aircraft structures. However, the use of thermosetting matrices imposes material limitations regarding recycling, malleability, and manufacturing-cycle times. The inverse hybrid laminate approach is based on a continuous fiber-reinforced thermoplastic matrix, in which a metal insert is integrated. For efficient manufacturing of the novel composites in high-volume production processes, conventional sheet metal–forming methods have been applied. It helped to reduce the cycle times and the costs of the forming equipment compared to currently used hybrid laminate-processing technologies. The present study analyzes the damage to the inverse hybrid laminate structures resulting from the interlaminar shear strength test. The tests were performed for eight laminate material configurations, which differed by the type and directions of the reinforced glass and carbon fibers in the polyamide matrix and the number of the fiber-reinforced polymer (FRP) layers in the laminates. Industrial computed tomography and scanning electron microscopy were used for analysis. Observed damages, including fiber–matrix debonding, fiber breakages, matrix fractures, interfacial debonding, and delamination in selected areas of the material, are strictly dependent on the laminate configurations. FRP layers reinforced by fibers perpendicular to the bending axis presented better resistance against fractures of the matrix, but their adhesion to the aluminum inserts was lower than in layers reinforced by fibers parallel to the bending axis.

Keywords: *interlaminar strength, fiber metal laminates, composite materials, hybrid laminates*

1. Introduction

Fiber metal laminates (FMLs) [1], also referred to as hybrid metal composites [2] or hybrid laminates [3], are materials combining polymer matrix composite laminates with fiber-reinforced polymers (FRPs) and metal sheets. They allow the synergy of the characteristics of the constituting materials: high ductility of the metal alloys and the strength of the composites [4]. They make it possible to reduce the weight of structures while maintaining high mechanical properties, especially fatigue strength [5]. FMLs are increasingly used in the construction of means of transport, mainly in the aerospace industry, but also in the automotive and railway industries [1]. They are part of a trend to systematically increase the share of composite materials in aircraft structures, e.g., for the new Airbus A350 XWB, the composite materials account for >50% of the aircraft weight [6]. Hybrid laminates developed for the aerospace industry were used in the fuselage of aircraft such as the Fokker F27 (aramid-reinforced aluminum laminate [ARALL]) and the Airbus A380 (glass laminate aluminum-reinforced epoxy [GLARE]) [7]. Currently, research is being conducted on the use of FMLs in the automotive industry due to the need to reduce fuel consumption [8], to reduce the weight of electric vehicles to compensate for the increase in the weight of batteries, or to increase passive safety by strengthening the structural components

* E-mail: mariusz.frankiewicz@pwr.edu.pl

© Frankiewicz et al. 2022. This is an open access article distributed under the Creative Commons Attribution-NonCommercial-NoDerivatives 4.0 License. (http://creativecommons.org/licenses/by-nc-nd/4.0/)

of passenger vehicles [9].

Despite the many advantages of FMLs, such as fatigue and impact resistance, damage tolerance, weight-saving capability, higher fire resistance, lower rates of corrosion (e.g., in comparison to Al alloys), these materials have their limitations related to lower stiffness, less industrialized manufacturing processes (besides aeronautical applications, FMLs are not widely applied), and limitations of the matrix polymers (usually thermostats) related to recycling and manufacturing-cycle times [10]. The matrix of FML materials used in the industry (GLARE, ARALL, and carbon-reinforced aluminum laminate [CARALL]) contain thermosetting materials (epoxy resins), which pose many problems with recycling [11]. FML solutions using thermoplastic polymers as the matrix are currently being developed: carbon fiber-reinforced polyamide aluminum laminate (CAPAAL) and carbon fiber-reinforced thermoplastic polyurethane aluminum laminate (CATPUAL). Further, polyamide (PA 6.6), polypropylene (PP), and polyether ether ketone (PEEK) are also used as matrix materials [12]. A significant benefit of using thermoplastics is the increased recyclability compared to duroplastics. Attempts to reduce the environmental impact of composites are also being undertaken with the aim to apply natural fibers, e.g., kenaf to produce kenaf fiber–reinforced composites (KFRC) and kenaf fiber—reinforced aluminum laminates (KeRALL) [13].

In addition to the development of the material structure of FMLs, work on them also includes the optimization of manufacturing processes. Classical technological processes used to manufacture components from FMLs, such as vacuum bagging or autoclave processes [7], are effective for small-series production, e.g., in the aerospace industry, but their application on a mass scale in, e.g., the automotive industry, is strongly limited [4]. With regard to select groups of thermoplastic matrix laminates, technologies such as deep drawing [14] or thermoforming processes [2] are being implemented to increase the manufacturing efficiency with a view to facilitate the mass production of FML components. This group of materials includes the InverTec inverted hybrid laminates with an inverted layup scheme compared to typical FMLs (e.g., GRALL or CARALL), as shown in Figure 1. The outer layers are made of FRP (PA sheets reinforced with carbon fibers [CFs] or glass fibers [GFs]) and a metallic liner is placed inside the laminate.

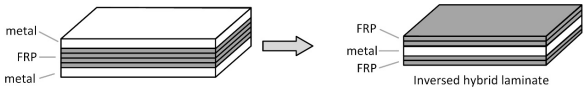


Fig. 1. Schematic comparison of fiber metal laminates: standard and inverse hybrid laminate (InverTec) [3]. FRP, fiber-reinforced polymer

An important characteristic of FMLs affecting their mechanical and performance characteristics [15] is the interlaminar cohesion, expressed as the interlaminar shear strength (ILSS). This parameter is one of the main material features influencing the possibility of forming FMLs by such processes as press brake bending or deep drawing [4]. ILSS can be tested by a number of methods, including the double-notch shear (DNS) test [16] and the three-point-bending load short-beam shear (SBS) test [17]. The last of the enumerated methods is currently used as a standard ILSS test according to American Society for Testing and Materials (ASTM) D2344 [15] and *Deutsches Institut für Normung* (DIN; German Institute for Standardisation) *Europaische Norm* (EN; European standard) 2563 or similar, used for high-modulus reinforced composites (International Organization for Standardization [ISO] EN ISO14130 [18]. In addition to shear stress analysis, scanning electron microscopy (SEM) images of damaged specimens are scrutinized to determine the characteristics of damage resulting from the SBS [15] and DNS [19] tests.

The aim of this study was to analyze more extensively the quality of the core–FRP interface in InverTec laminate variants based on the assessment of defects in InverTec laminate specimens formed during ILSS tests, described in a previous work by the author [3], carried out with the three-point bending SBS method and comparison with defects arising during ILSS tests in FMLs with a classic ply arrangement. Due to the attempts to develop

Table 1. Configuration of the analyzed series of FMLs

Series	Configuration of FRP laminate layers	Laminate code (variant 0°)	Laminate code (variant 90°)
S1	3x CFR-TP PA6GF60	$[0^G/90^G/0^G/\text{Alu}]_s$	$[90^G/0^G/90^G/\text{Alu}]_s$
S2	3x CFR-TP PA6GF60	$[0^G_3/\text{Alu}]_s$	$[90^G_3/\text{Alu}]_s$
S3	1x CFR-TP PA6CF60/4x- CFR-TP PA6GF60	$[0^C/0^G_4/\text{Alu}]_s$	$[90^C/90^G_4/\text{Alu}]_s$
S4	1x CFR-TP PA6CF60/4x- CFR-TP PA6GF60	$[0^C/90^G/0^G/90^G/0^G/\text{Alu}]_s$	$[90^C/0^G/90^G/0^G/90^G/\text{Alu}]_s$

CFR-TP, carbon fiber-reinforced thermoplastic; GF, glass fiber; FML, fiber metal laminate; FRP, fiber-reinforced polymer; PA, polyamide

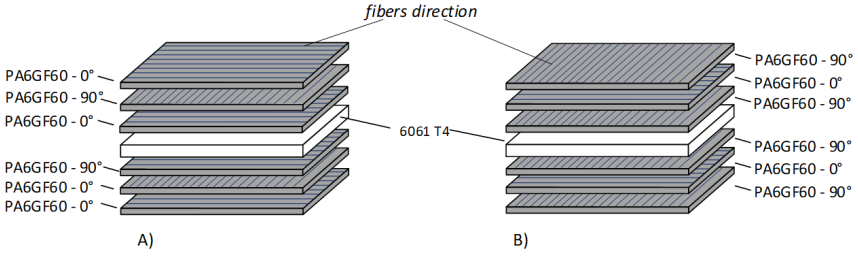


Fig. 2. Example of fiber arrangement in S1 series laminates: variant 0° (S1.0) **(A)** and variant 90 (S1.90) **(B)**. GF, glass fiber; PA, polyamide

Table 2. Parameters of variothermal consolidation of InverTec inverted laminate sheets

Steps	Pressure (bar)	Temperature (°C)	Time (min)
Heating and plasticizing of polymer matrix	20	260	6.5
Consolidation of the FRP composite	30	260	3.5
Cooling phase and solidification of the polymer melt	30	60	16.5

FRP, fiber-reinforced polymer

inversed laminates for mass production, e.g., in the automotive industry, the analysis of defects arising during ILSS tests has also been used as a method to assess the possibility of forming InverTec laminates by drawing processes. Thus, this work is a continuation and extension of the authors' own research results published earlier.

2. Materials/technology

The test specimens were made from an inverse hybrid laminate, the layers of which were made from FRP prepregs, Ticona Celstran PA6-CF60 0.15 mm and PA6-GF60 0.29 mm, containing 60% by weight of CFs or GFs in the PA 6 matrix, and a 1 mm thick sheet of 6061-T4 aluminum alloy. The 6061 alloy sheet was grit-blasted before consolidation with the remaining laminate layers in order to increase the adhesion of its surface to the FRP layers.

Eight laminate configurations were adopted for the analysis: four ply arrangements, made with two variants of fiber arrangement, as detailed in Table 1 and Figure 2.

As shown in Table 1, the two variants of series S2 were unidirectional (UD) laminates, while the other variants of series S1, S3, and S4 were cross-ply laminates.

The laminate sheets were made by variothermal consolidation using a Colin P300 press. The process diagram is shown in Figure 3, and the process parameters are presented in Table 2.

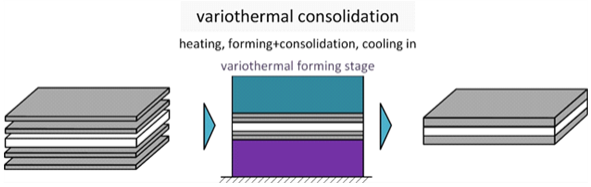


Fig. 3. Diagram of the process of forming an inverted hybrid laminate (InverTec)

3. Tests of specimens

Specimens with dimensions 20 mm × 10 mm were subjected to a three-point-bending load SBS test in accordance with DIN EN 2563. The view of the SBS test is shown in Figure 4. The test conditions are given in Table 3.

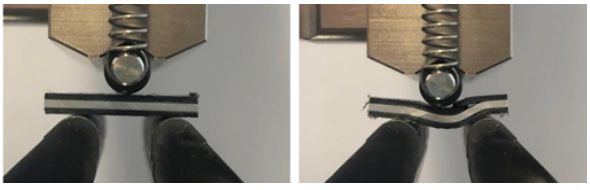


Fig. 4. View of the ILSS test using a three-point-bending load (short beam test) [3]. ILSS, interlaminar shear strength

Table 3. Parameters for the ILSS SBS test

System	Zwick\Roel 5.0
Temperature	23°C
Humidity	46%
Test speed (constant)	2 mm/min
Span length	8 mm
Bending die	5 mm
Support rollers	2 mm

ILSS, interlaminar shear strength;
SBS, short-beam shear

The research described in this article extends the results of analyses presented by the author in an earlier publication [3], which presents the results of the ILSS test in the form of the measured shear stresses (τ_{max}, τ_B) in the specimens described in Table 1. The results of the ILSS SBS test are given in Table 4. Due to the variations in the fiber arrangement in the FRP layers, which strongly influence the measured characteristics, the results of

Table 4. Mean values of shear stresses τ_{max} and τ_B determined by the ILSS SBS test for laminates listed in Table 3 [3]

	τ_{max} [MPa]		τ_B [MPa]	
	Configuration			
Series	0	90	0	90
S1	33.3	48.5	26.6	40.0
S2	49.6	20.7	44.2	16.0
S3	57.3	20.3	46.8	17.4
S4	52.6	41.7	42.7	35.6

ILSS, interlaminar shear strength;
SBS, short-beam shear;
τ_{max}, maximum shear stress;
τ_B, shear stress at the moment of first failure

the ILSS test of the specimens were compared in two groups for the variants 0 and 90. Summarizing the obtained results of shear stress values measurements (τ_{max}, τ_B), one can state as follows:

- Specimens of variant "0" showed the highest shear stresses for Series 3, $[0^C/90^G{}_4/\text{Alu}]_s$, amounting to τ_{max} = 57.3 MPa and τ_B = 46.8 MPa. The lowest values of shear forces, lower by >40% compared to the 3/0 series, were obtained for the specimens of Series 1 (τ_{max} = 33.3 MPa; τ_B = 26.6 MPa);
- Specimens of variant "90" showed the highest shear stress for Series 1 (τ_{max} = 48.5 MPa and τ_B = 40.0 MPa). The lowest ILSS results were obtained for Series 2 (τ_{max} = 20.7 MPa; τ_B = 16.0 MPa) and Series 3 (τ_{max} = 20.3 MPa; τ_B = 17.4 MPa). For Series 2 and Series 3, the achieved shear stresses between the layers were lower by >50% compared to the results for Series 1.

The ILSS is closely associated with the type of additional surface treatment applied to the metallic layers (e.g., Al, Ti, or steel alloys) and to the adhesion layers between the metallic and FRP sheets. The obtained ILSS values of InverTec laminates are similar to the results of studies on FMLs with a similar, inverted, carbon fiber-reinforced polymer (CFRP)/Al ply arrangement presented by Bellini et al. [20]. They analyzed the effect of additional

adhesive layers on the ILSS of laminates produced using a vacuum bag process, obtaining shear strengths of 39–49 MPa. The research carried out by Bieniaś et al. [18] presented the ILSS values in the range of 81.5–93 MPa for CARALL laminates with classical Al/CFRP/Al ply arrangement, produced by the autoclave method, in which aluminum alloy layers were additionally subjected to chromic acid anodizing (CAA) and additional adhesive primer coating.

Damage analysis of the specimens was carried out using industrial computed tomography (CT) and SEM methods. CT examinations were performed using the Zeiss Metrotom CT system (CARL ZEISS, Oberkochen, Germany). Scanning/reconstruction data obtained were as follows: voxel size: 30 μm; voltage: 120 kV; current: 200 μA; integration time: 2 s; filter: Cu 0.25 mm; number of projections: 850. Microscopic observations were performed using a Zeiss Evo MA 25 scanning electron microscope.

4. Results and discussion

4.1. Analysis of images of specimens obtained by CT

Images of the specimens obtained with CT are shown in Figure 5. The columns contain views of the laminate specimens of variants 0 and 90, while the rows correspond to the consecutive series of specimens S1–S4. The damage to the specimens within the specimen variants was of a similar type, which was also confirmed by the SEM analyses presented later in this article. In Variant 0 (left column), the debonding delaminations of the glass fiber–reinforced polymer (GFRP) layers and the Al alloy core were the decisive type of damage. In the case of specimens S1 and S2, (i) interlaminar shear failures manifested by end openings are visible, which caused separation of the GFRP layers from the Al alloy core on almost half of the lower surface of the core, marked by the arrows (i) on Figure 5; local shear debonding [arrows (ii)] is also visible in these specimens. The damage types are, besides shear misalignment, characteristic defects formed in FMLs under pure shear stress [17]. Similar defects are presented for GLARE materials [15], in which debonding failure occurred near the neutral layer. In the InverTec laminate specimens analyzed, this layer was located in the Al core. It occurred mainly in the specimens of Variant 0 due to the influence of the longitudinal fibers reinforcing the FRP layer. Higher damage and deflection of specimens with a higher number of transverse reinforced layers (Variant 90) in relation to specimens with longitudinal fibers confirms the results of observations made earlier, e.g., in relation to GLARE-type laminates, as shown by Bahari-Sambran [21]. The high stiffness of FRP layers with longitudinal fibers resulted in high intrinsic shear stresses at the FRP–core interface and, consequently, in the separation of the FRP layers from the core of Series S2.0 specimens after the test was completed, and the specimens were removed from the test stand.

For Variant 90 (Figure 5, right column), the decisive damage type was matrix cracks. Their nature corresponded to the defects produced by SMS tests in GLARE laminates [15]. Moreover, asymmetric deflections of specimens of Series S4–S90 (Figure 5) occurred during the SBS tests of GLARE specimens.

In addition to the damage characteristic of shear stress in the form of FRP–core delamination, damage due to bending stresses resulting from the three-point-bending load SBS test was also observed in the analyzed specimens. The bending stresses caused stretching or compression of the laminate layers located above or below the neutral layer. The resulting matrix damage was more visible in the SEM images.

The behavior of the specimens was mainly related to the arrangement of fibers in the FRP layers. When their direction corresponded to the direction of tensile/compressive stresses in the laminate layers, for Variant 0, the loads were mainly transmitted through the fibers. For Variant 90, the loads were mainly transmitted through the matrix of the FRP layers, which resulted in its cracking.

Delaminations, combined with springback defects, are most evident in Variant 0 specimens, wherein the fiber direction is perpendicular to the bending line.

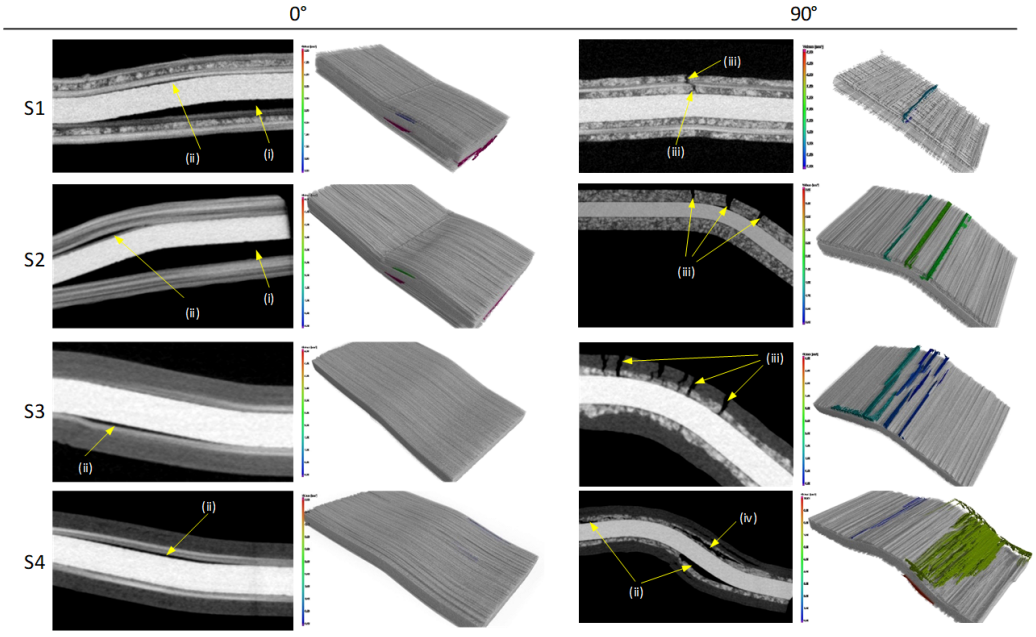


Fig. 5. Cross-sectional views and 3D images obtained with CT of series S1–S4 specimens in Variants 0 and 90. Colored areas on 3D images indicate damages caused by delaminations and cracks in the matrix. Defects marked on the images: springback damage (i), core and FRP delaminations (ii), matrix cracks in FRP layers in planes parallel to the bending axis (iii), and matrix cracks in planes perpendicular to the bending axis (iv). CT, computed tomography; FRP, fiber-reinforced polymer

One cause of the failure of FMLs subjected to bending may be the transverse distributed residual stresses causing elastic deformation/springback in UD fiber-reinforced composites [22]. As is visible in Figure 5, for specimens of the Series S1.0–S2.0 (Variant 0), separations of the FRP layers from the core (i) were formed after the tests due to the residual stresses of UD-reinforced GFRP layers [23]. The damage to the Specimens S3.0 and S4.0, as seen in Figure 5, are smaller than for specimens S1.0/S2.0.

In the specimens of Variant 90, the predominant damage type was matrix cracks running across the FRP layers in planes parallel to the bending axis. Due to the ILSS tests performed with SBS, the deflections of the laminate layers were of the same type as those seen during bending [24]; in the outer layers, they are caused by compression (indenter side) or tension (support side). Due to the course of the fibers in the Variant 90 specimens, the stresses and strains of the FRP layers occurred across the direction of the reinforcing fibers. This resulted in matrix damage in the layers subjected to tensile stresses, marked as (iii) in Figure 5. The largest matrix cracks in the planes parallel to the bending axis were observed in specimens S1.90, S2.90, and S3.90, in which the number of transversely reinforced FRP layers was greater than the number of longitudinally reinforced layers.

Industrial CT allowed the damage analysis of the specimens in cross section, without the need to perform a series of blanks. Thus, the main types of defects caused by ILSS SBS tests were observed: cracks in the matrix and delaminations of FRP layers and laminate core. Due to the imaging resolution, i.e., a voxel size of 30 μm, it was not possible to examine the nature of the fiber and the matrix defects in detail. These analyses were carried out using SEM.

4.2. SEM analysis of specimens

Due to the conditions of ILSS tests conducted with the three-point-bending load SBS test, in the analyzed specimens, there were also compressive

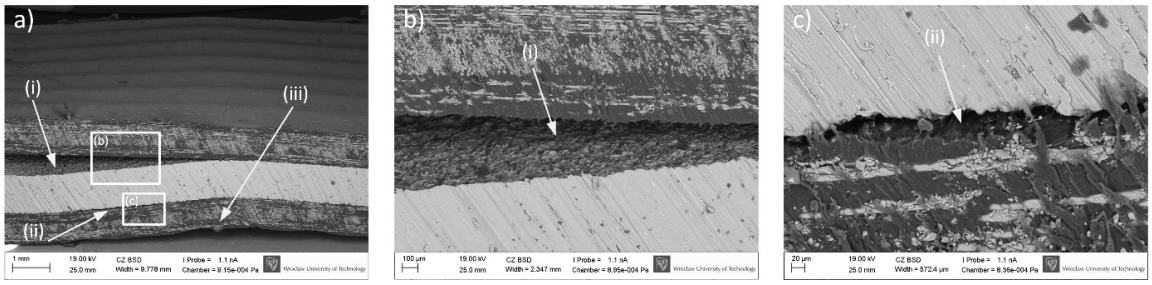


Fig. 6. Views of the defects observed at the interface between the FRP and the Al6061 layers of series S1.0 specimens: detachment of FRP layers (i), slight delamination on the core surface (ii), and fiber bulking (iii). The areas marked within the squares are shown at different magnifications (B and C). The cross section seen is in the plane perpendicular to the bending line of series S1 specimen 0 (S1.0), as observed by SEM/BSD. FRP, fiber-reinforced polymer; SEM/BSD, backscattered electron detector-based scanning electron microscopy

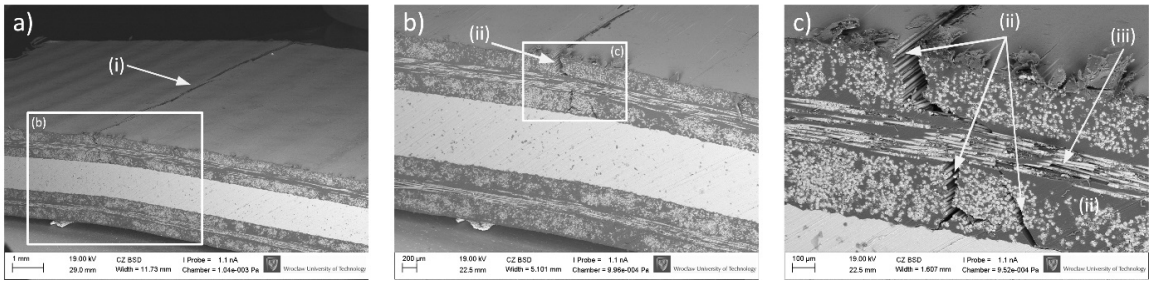


Fig. 7. Views of defects observed in series S1.90 specimens: matrix cracks (i) and (ii); GF cracks (iii). The indicated areas are shown at different magnifications (B and C). The cross section is in the plane perpendicular to the bending line of series S1.90 specimen, as seen by SEM/BSD. GF, glass fiber; SEM/BSD, backscattered electron detector-based scanning electron microscopy

and tensile stresses in addition to shear stresses. Their effect was evident in the types of damage observed during the analysis of SEM images of the specimens.

Delaminations between the FRP layers and the aluminum core were observed in series S1.0 specimens. They occurred on both sides of the specimen (Figure 6A) but were most prominent on the side of the layers subjected to tensile load (Figure 6B). A pronounced delamination occurred on almost half of the specimen surface, indicated as (i) in Figures 6A and 6B. In the layers subjected to compression, visible below the core, small delaminations were observed between the core and the FRP, denoted as (ii) in Figure 6C, and bulking (iii) in Figure 6A. The images of the analyzed specimens show no damage to the FRP layers in the form of delamination and matrix cracking. Each of the specimens of series S1.0 showed the same type and extent of damage. The analyzed specimens showed similar damage as in GLARE [15] or Ti/CF/PMR PA FMLs [25]. A significant influence on the behavior of this laminate is the inherent stresses introduced into the laminate layers during the molding process [26].

In the case of series S1.90 specimens, matrix cracks were observed running along the fibers reinforcing the FRP sheets in the outer laminate layer under tension (i), as shown in Figure 7A, and cracks (ii) and (iii) in Figures 7B and 7C. Cracks (ii) were propagated in the two FRP layers subjected to tensile load (Figure 7C). They were not present in the specimens of series S1.0, in layers with the same fiber direction. In the images in Figures 7A and 7B, no delamination was observed between the Al alloy sheet and the FRP

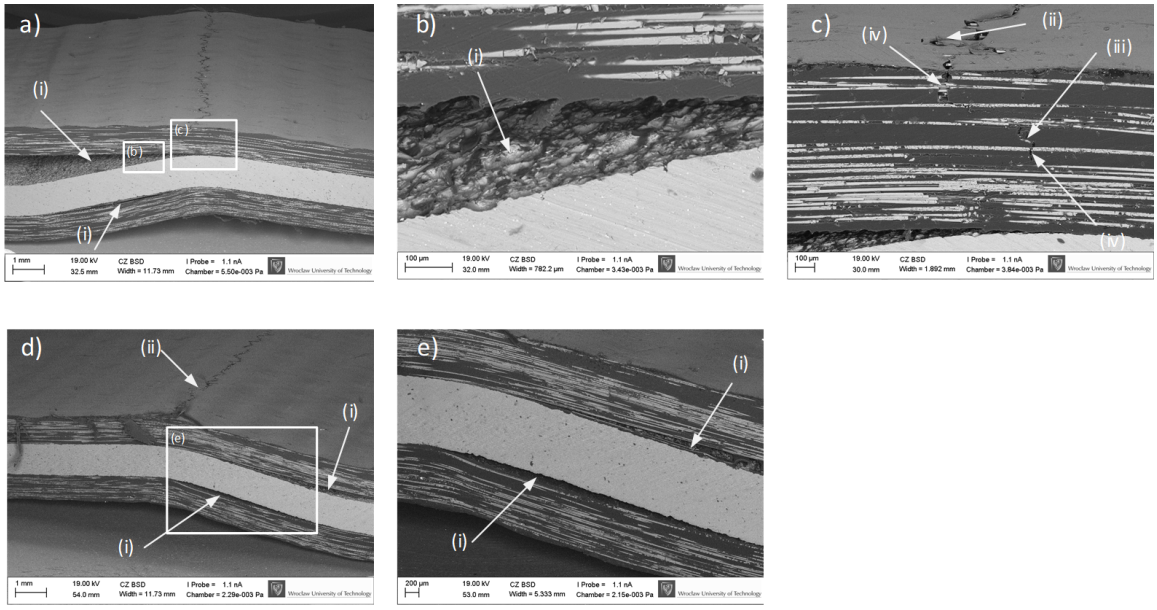


Fig. 8. Views of defects in series S2.0 specimens: delamination (i), matrix cracks (ii) and (iii), and GF cracks (iv). The indicated areas are shown at different magnifications (B, C, E). Cross section is in the plane perpendicular to the bending axis of the specimens, observed by SEM/BSD. GF, glass fiber; SEM/BSD, backscattered electron detector-based scanning electron microscopy

layers, which was due to the higher ductility of the composite layers. Due to the presence of two layers with GFs running in the 0° direction and four FRP layers with fibers directed at 90°, the stresses in the FRP layers were mainly transmitted through the matrix. Therefore, the arrangement of the FRP layers in series S1.90 specimens, which was due to their matrix susceptibility, was characterized by higher ductility. The type of the damage corresponds to the defects observed in the bending of GLARE-type FMLs [27]. The damage to the GFRP layers occurred as a result of fiber–matrix debonding, which coincides with the results of previous research work carried out using SBS tests on cross-ply GLARE laminates [17]. This defect type was also observed during three-point bending tests on CARALL laminates [28]. This damage mechanism was characteristic of all 90 series laminates (Sx.90).

A similar type of damage to that of series S1.0 can be observed in a series S2.0 specimen (Figure 8). The delamination formed between the Al core and the FRP layer (i) can be seen on both sides of the core (Figure 8A, 8B, 8D, and 8E). However, the extent of damage varied between the specimens of this series (Figure 8A and Figure 8D, 8E). The defects included matrix cracks (ii) and (iii), running perpendicular to the fiber direction. Cracks were also observed in the GFs (iv) in the outer layers subjected to tensile deflection (Figure 8C). They were a defect typical of S2.0 specimens. Literature analyses indicate that this type of defect appears during ILSS tests of GLARE laminates [15]. In the case of the analyzed inverted laminate, in the specimens of series S1.0 and S2.0, the visible detachments of FRP layers from the laminate core occur almost in the middle of the FRP–Al alloy core interface (Figure 8A). Due to the higher forming temperatures of InverTec laminates, compared to FMLs with a thermosetting matrix such as GLARE, their FRP layers had a higher level of residual stress and associated elasticity, which affected the separation of the laminate layers (i) (Figure 8A). In a part of the series S2.0 specimens, only slight delamination was observed on the surfaces on both sides of the core (Figure 8D), which could be related to the temperature stability of the forming process of the inverted laminate specimens.

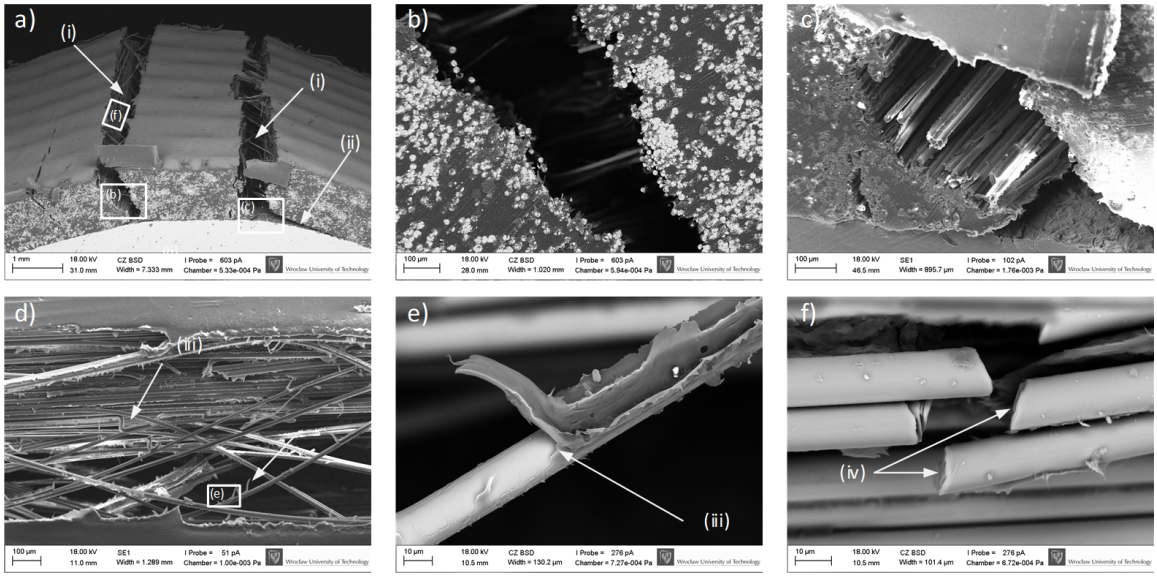


Fig. 9. Views of the damage to the series S2.90 specimens: matrix cracks (i), FRP and laminate core delamination (ii), matrix and GF delamination (iii), and GF cracks (iv). The indicated areas are shown at different magnifications (B–F). Cross section is in the plane perpendicular to the bending axis of the specimens, observed by SEM/BSD. FRP, fiber-reinforced polymer; GF, glass fiber; SEM/BSD, backscattered electron detector-based scanning electron microscopy

The series S2.90 specimens were characterized by significant matrix damage (Figure 9A). Matrix cracks occurred along the fiber directions in the FRP layers (i) (Figure 9A, 9B, 9E). Clear separation of the fiber surface from the matrix was evident (iii) (Figures 9B–9D) and fiber cracks (iv) (Figure 9F). Specimens of this series showed the lowest ILSS value [3]. The nature of the damage to the specimens of this series was similar to that of the FRP layers in series S1.90, but due to the lack of longitudinal fibers, the extent of damage was much greater and ran along all the FRP layers subjected to tensile load. Despite the test with a short *l*/*h* ratio (*l* – the span of the supports; *h* – the height of the specimen), bending failure occurs (Figure 9) in the form of matrix cracks (i), which in the case of GLARE laminates start to appear for *l*/*h* ratios above ~16 [27]. A similar type of failure also occurred for specimens of the series S3.90.

The series S3.0 specimens exhibited significant delamination of the FRP and aluminum sheet layers in the laminate core (iii) (Figure 10A, 10B). In the area of laminate layers subjected to compressive stress (Figure 10C), slight bulking of the fibers was observed. No cracks were observed in the PA6 matrix (Figure 10B, 10C, 10D). As with the earlier specimens of Variant 0, the delamination was caused by the stiffness of the FRP layers. The plastic deformation of the PA6 matrix (v), visible in Figure 10E, formed during separation from the surface of the Al core, proves that the delamination was caused by detachment of layers from the substrate as a result of the elastic deformation forces of the FRP layers running perpendicular to the substrate. Cracks in the GFs were also visible in the GFRP layers subjected to tension (Figure 10E). Small matrix cracks ran along the CFs on the outer surface of the laminate (i).

The damage to the series S3 specimens of Variant 90 was among the largest of all the Variant 90 specimens. Significant cracks in the matrix (i) and (iii) (Figures 11A–11D) in the zone subjected to tensile load run through all the laminate layers in this area. Their type is similar to the damage observed for the series S2.90 specimens (Figure 9). They result mainly from the direction of fiber orientation in the CFRP/GFRP layers and thus from the stress transfer through the PA6 matrix without

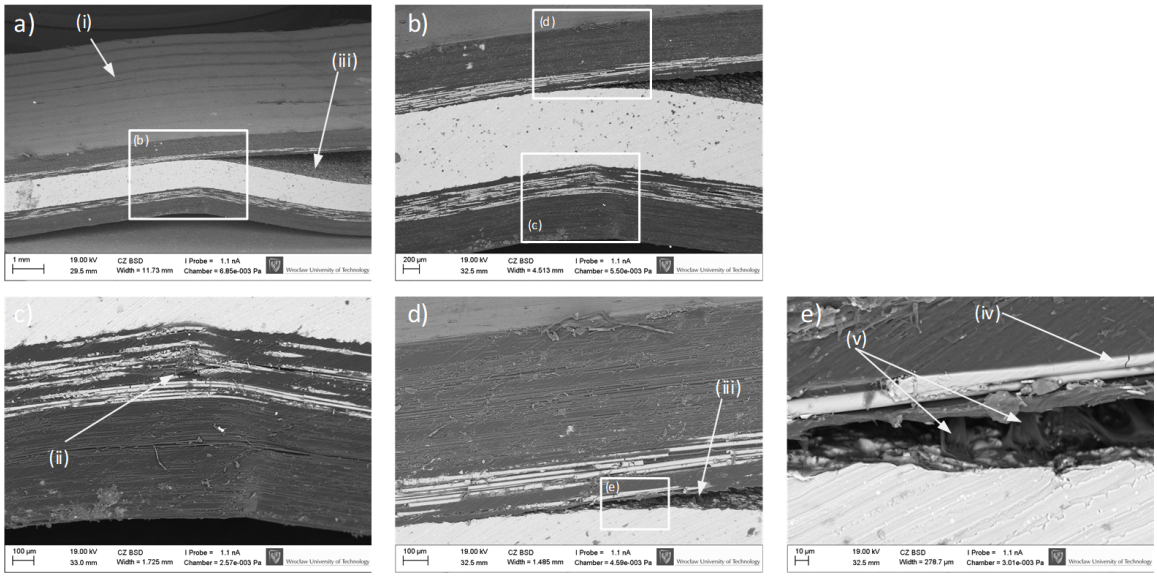


Fig. 10. Views of the damage to the series S3.0 specimens: cracks on the laminate surface (i), bulking of GFs (ii), delamination of GFRP layers from the core (iii), and cracking of GFs (iv). The indicated areas are shown at different magnifications (B–E). Cross section is in the plane perpendicular to the bending axis of the specimens, viewed using SEM/BSD. GF, glass fiber; GFRP, glass fiber–reinforced polymer; SEM/BSD, backscattered electron detector-based scanning electron microscopy

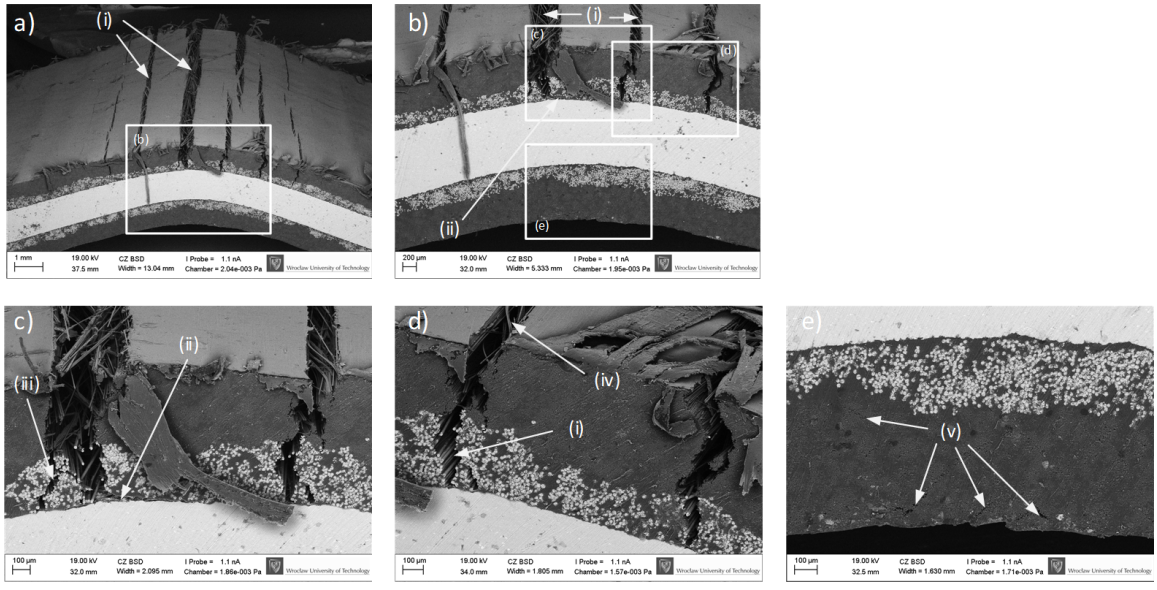


Fig. 11. Views of damage to the series S3.90 specimens: PA matrix cracks (i); delamination of GFRP layers from the core (ii); delamination of GFs and PA matrix (iii) and (iv); and PA matrix cracks in the CFRP layers (v). The indicated areas are shown at different magnifications (B–E). Cross section is in the plane perpendicular to the bending axis of the specimens, as observed by SEM/BSD. CFRP, carbon fiber-reinforced polymer; GF, glass fiber; GFRP, glass fiber-reinforced polymer; PA, polyamide; SEM/BSD, backscattered electron detector-based scanning electron microscopy

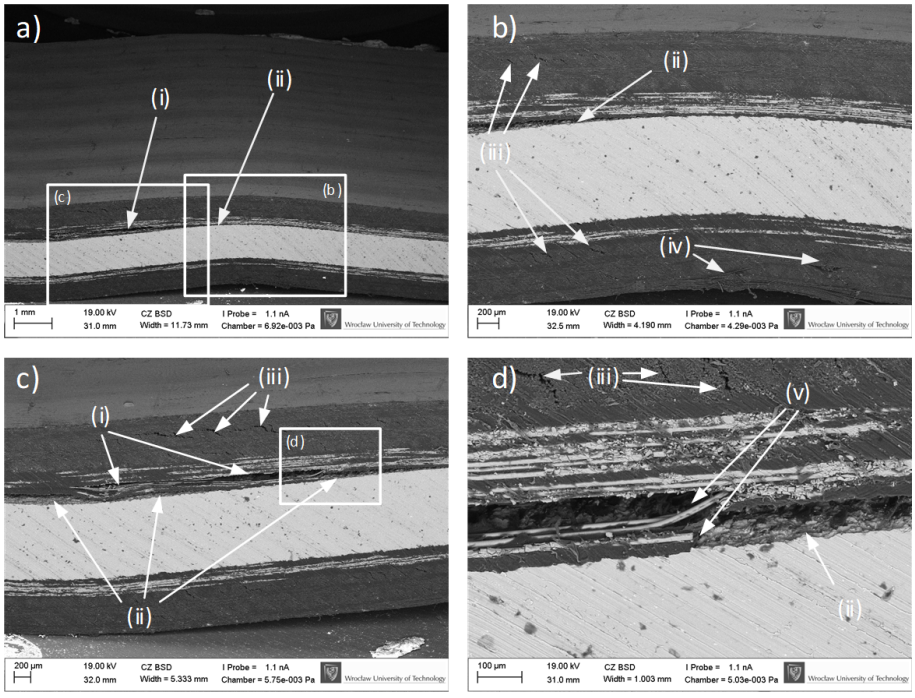


Fig. 12. Views of damage to series S4.0 specimens: cracks in GFRP layers (i), delamination of GFRP layers from the core (ii), PA matrix cracks and fiber delamination in CFRP layers (iii), PA matrix cracks and CF bulking (iv), and GF cracks (v). The indicated areas are shown at different magnifications (B–D). Cross section is in the plane perpendicular to the bending axis of the specimens, viewed using SEM/BSD. CF, carbon fiber; CFRP, carbon fiber-reinforced polymer; GFRP, glass fiber–reinforced polymer; PA, polyamide; SEM/BSD, backscattered electron detector-based scanning electron microscopy

the participation of CF/GF. Small cracks in the matrix are also visible in the area subjected to compressive stress in the surface layer of the laminates (v) (Figure 11E). Only minor delamination between the core and the remaining laminate layers is observed (ii).

Delaminations were observed on the surface of the laminate core (ii) in specimens of the series S4.0. Their type differed from the damage of previous series of specimens of Variant 0. Delaminations were locally present (Figures 12A and 12C). Moreover, delaminations were also present in the FRP layer, not only at the FRP–core laminate boundary (Figure 12D). This behavior may be indicative of a lower level of residual stress in the FRP layers, resulting from a higher number of alternating laminate layers [23]. Additionally, matrix cracks were observed in the CFRP layers, formed by separation of the matrix from the fibers (iii) (Figures 12B and 12D). The cracks formed in the areas of the layers subjected to both tensile and compressive stresses (Figures 12B–12D) and involved fibers arranged in the direction of 90° [(iii) and (iv)]. Their propagation was stopped by layers with fibers running in the direction of 0° (Figure 12D) due to the alternating arrangement of the layers. In addition to cracks in the matrix itself (i), interrupted GFs (v) were visible (Figure 12D).

Delamination and matrix cracks were observed in the series S4.90 specimens (Figure 13). The delaminations occurred in the GFRP layers immediately adjacent to the aluminum core of the laminate (Figure 13A, 13B). Delaminations of the compression layers (iii) have also been observed previously in the analysis of bending-induced FML CARALL damage [29]. The experimental and finite element modeling (FEM) bending analyses of CARALL laminates, described in a previous paper [29], show that compressive stresses in the outer layers of the laminate, when reaching their failure stress limits,

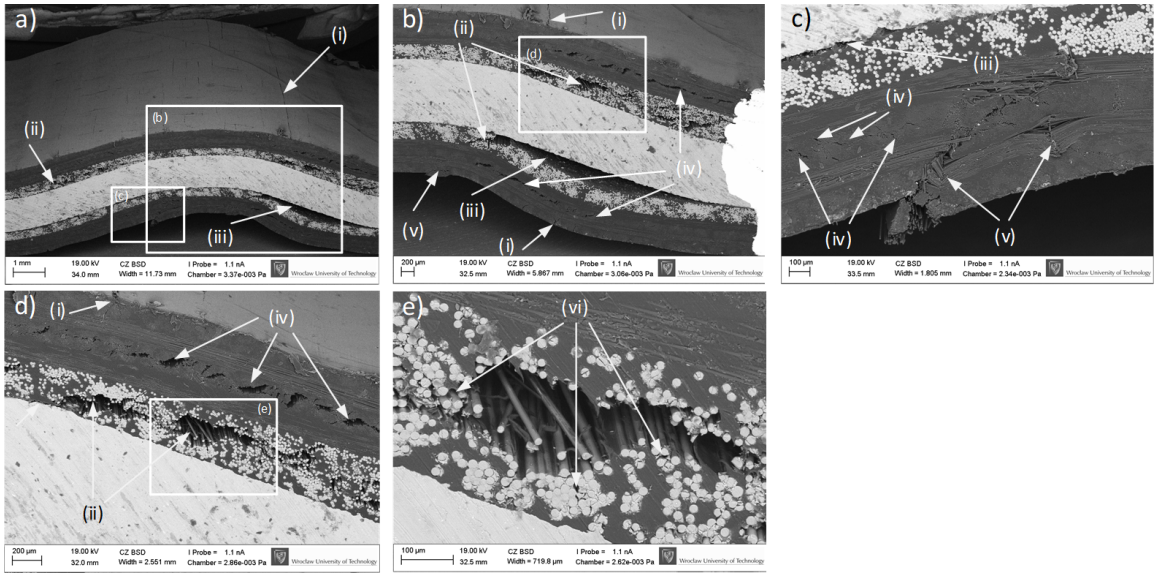


Fig. 13. Views of damage to the series S4.90 specimen: surface cracks in CFRP layers (i), cracks in GFRP layers (ii), delamination of GFRP layers and core (iii), PA matrix cracks and fiber delamination in CFRP layers (iv), CF bulking (v), and delamination of PA matrix and fibers in GFRP layers (vi). The indicated areas are shown at different magnifications (B–E). Cross section is in the plane perpendicular to the bending axis of the specimens, viewed using SEM/BSD2. CF, carbon fiber; CFRP, carbon fiber–reinforced polymer; GFRP, glass fiber–reinforced polymer; PA, polyamide; SEM/BSD, backscattered electron detector-based scanning electron microscopy

Table 5. Summary/classification of damage in laminate plies in relation to ply fiber orientation and stress distribution

Type of load		**Tension**		**Compression**	
FRP layer fiber arrangement		0	90	0	90
Type of damage		**Presence in specimens S.1/S.2/S.3/S.4**			
GFRP–core delaminations		+/+/+/+	–/+/±	±/–/–	–/–/–/+
Cracks on the external surface of the laminate		–/+/±	+/+/+/+	–/–/–/–	–/–/+/+
Matrix cracks	GFRP	–/–/–/+	+/+/+/+	–/–/–/+	–/–/–/+
	CFRP	n.e./n.e./+/+	n.e./n.e./–/+	n.e./n.e./+/+	n.e./n.e./+/+
Fiber cracks	GFRP	–/+/±	–/–/–/–	–/–/–/–	–/–/–/–
	CFRP	n.e./n.e./–/–	n.e./n.e./–/–	n.e./n.e./–/–	n.e./n.e./–/–
Fiber bulking	GFRP	n.a.*		±/±	±/±
	CFRP	n.a.*		n.e./n.e./–/+	n.e./n.e./–/+

Legend: "–" indicates not observed; "+" indicates observed;
"n.e.": CFRP layer was not existing in the analyzed configuration of specimen.
n.a.*: bulking can be connected to the compressed plies only.
CFRP, carbon fiber-reinforced polymer; FRP, fiber-reinforced polymer;
GFRP, glass fiber–reinforced polymer

initiate fiber bulking and matrix cracking, as well as plastic deformation of the laminate surface layers, leading to the delaminations seen in Figure 13B. In layers subjected to compression, bulking of the CFRP layers was detected (Figure 13C). Matrix cracking, as in the case of specimens of this series,

observed in Variant 0, occurred in layers with CFs and GFs arranged transversely,i.e., perpendicular to the longer edges of the specimen (Figures 13D and 13E). The size of damage from the ILSS test, for specimens of the series S4.90, was significantly greater than that for specimens of the same series in Variant 0 (Figures 13B and 13D). The matrix cracks did not propagate across the CFRP layers, due to the alternation of CF in consecutive layers (0° and 90°) (Figure 13D). Similarly, matrix cracks of GFRP (transversely reinforced FG) did not propagate to the adjacent CFRP layers due to the longitudinal arrangement of the CFs (Figure 13D). Matrix cracks were observed on the outer surface of the specimens, running along the direction of the fibers reinforcing the FRP layer.

A summary of the types of damage observed in the laminate specimens is presented in Table 5. The damage type depended on the configuration of the laminate layers: the type of fibers (prepregs) used, the direction of their arrangement, and the number of FRP layers. The layers of prepregs with fibers arranged longitudinally (variant 90) exhibited matrix cracks because, in their case, the direction of loading was across the reinforcing fibers and therefore the stresses were transmitted through the matrix without fiber involvement. In the case of variants of laminates with longitudinal FRP layers (Variant 0), the main type of damage was delamination of the FRP layers from the surface of the aluminum alloy insert, as well as within the FRP layers, mainly GFRP.

5. Conclusions

The aim of this study was to analyze the defects in InverTec laminates occurring during ILSS tests carried out using the three-point bending SBS method. Based on the type, size, and extent of the defects, the quality of the laminate fabrication was assessed in terms of the durability of the interface between the core and the FRP layers. The stability of the interface between the laminate layers is particularly important from the point of view of processing methods of the analyzed material in the automotive industry.

Tests were carried out for eight sets of specimens, four types of laminate ply configurations, differing in the type of reinforcing fibers used (GF/CF) of the PA matrix and the number of FRP layers, in two variants of fiber direction orientation each. Based on these, the following conclusions were drawn:

- The damages—including peeling of reinforcing fibers from the matrix, fiber cracks, fiber bulking, matrix cracking, delamination between the aluminum core and the FRP layers of the laminate—occurred locally and their location was closely related to the structure of the laminate.
- The greatest damage occurred in specimens with FRP layers reinforced with fibers in the direction of 90°, parallel to the bending axis in the ILSS test, corresponding to the "90" variant. In this case, the load was mainly transmitted through the matrix, which resulted in cracks in its structure. In specimens S2.90 and S3.90, the largest defects were observed. At the same time, these specimens had the lowest values of interlaminar shear strength.
- Cracks appearing in FRP 90 layers were partially limited when there were several FRP layers in the laminate structure running in the direction of 0°, e.g., for specimens S1.90 and S4.90. In this case, the number of FRP 0 plies influenced the extent of cracks in the FRP 90 matrix.
- For FRP layers arranged at an angle of 0°, the fibers in the reinforcement prevented matrix cracking. However, the high stiffness of the FRP 0 plies caused flexural deflection during the test, which, combined with the plastic deformation of the aluminum sheet in the core, resulted in delamination of the plies.
- The behavior of FRP plies during ILSS testing may also have been influenced by the inherent stresses developed during the forming/consolidation of the laminates. The impact of residual stresses in GFRP/CFRP layers on the interlaminar strength of hybrid

laminates and the possibility of using other methods to increase adhesion to the aluminum core surface should be further investigated in future work.

- Based on the high stiffness of the layers oriented at angle 0° (configuration "0") and the shear stress level obtained for laminates consisting of GFRP and CFRP layers, the use of InverTec laminates with a structure represented by the series S3.0 is recommended for components loaded mainly in one direction. An example of an element in which the recommended laminate structure was validated was the cross member of the car body roof. This type of component was used as a demonstrator within the InverTec project. The static bending and impact tests showed that the composite demonstrator part presented the same stiffness as the monolithic steel reference, with >40% weight reduction. Furthermore, the delamination of the aluminum alloy core and FRP layers for the demonstrator part was reduced by surface treatment of the core and the use of additional PA6 adhesive plies.

Acknowledgements

The presented studies were performed as part of a CORNET/22/3/2016 project titled "Load optimized inverse composite technology InverTec" and supported by the National Centre for Research and Development (NCBR) in Poland and Industrial Collective Research (IGF) in Germany and European Research Association for Sheet Metal Working (EFB) to explore integrative in-mold processes with plastic/metal composites. Financial support is gratefully acknowledged.

References

[1] Kavitha K, Vijayan R, Sathishkumar T. Fibre-metal laminates: a review of reinforcement and formability characteristics. Mater Today Proc. 2020;22:601–5.

[2] Drossel WG, Riemer M, Scholz P, Osiecki T, Kroll L, Frankiewicz M, et al. Forming induced interface structures for manufacturing hybrid metal composites. CIRP Ann. 2020;69(1):253–6.

[3] Osiecki T, Gerstenberger C, Timmel T, Frankiewicz M, Dziedzic R, Scholz P, et al. Inverse hybrid laminate for lightweight applications. Key Eng Mater. 2020;847:40–5.

[4] Ding Z, Wang H, Luo J, Li N. A review on forming technologies of fibre metal laminates. Int J Light Mater Manuf. 2021;4(1):110–26.

[5] Stefaniak D, Prussak R. Chances and challenges in the application of fiber metal laminates. Adv Mater Lett. 2019;10(2):91–7.

[6] Zhang X, Chen Y, Hu J. Recent advances in the development of aerospace materials. Prog Aerosp Sci. 2018;97:22–34.

[7] Botelho EC, Silva RA, Pardini LC, Rezende MC. A review on the development and properties of continuous fiber/epoxy/aluminum hybrid composites for aircraft structures. Mater Res. 2006;9(3):247–56.

[8] Heggemann T, Homberg W. Deep drawing of fiber metal laminates for automotive lightweight structures. Compos Struct. 2019;216(February):53–7.

[9] Bambach MRR. Fibre composite strengthening of thin steel passenger vehicle roof structures. Thin-Walled Struct. 2014;74:1–11.

[10] Vermeeren CAJR. An historic overview of the development of fibre metal laminates. Appl Compos Mater. 2003;10(4–5):189–205.

[11] Zopp C, Dittes A, Nestler D, Scharf I, Kroll L, Lampke T. Quasi-static and fatigue bending behavior of a continuous fiber-reinforced thermoplastic/metal laminate. Compos Part B Eng. 2019;174(June) , p.107043.

[12] Nestler D, Trautmann M, Nendel S, Wagner G, Kroll L. Innovative hybride Laminate aus Aluminiumlegierungsfolien und faserverstärkten thermoplastischen Schichten. Materwiss Werksttech. 2016;47(11):1121–31.

[13] Osman E, Rashid MWA, Abd Manaf ME, Moriga T, Kamarudin H. Influence of hygrothermal conditioning on the properties of compressed kenaf fiber/epoxy reinforced aluminium laminates. J Mech Eng Sci. 2020;14(4):7405–15.

[14] Heggemann T, Homberg W, Sapli H. Combined curing and forming of fiber metal laminates. Procedia Manuf. 2020;47(2019):36–42.

[15] Liu C, Du D, Li H, Hu Y, Xu Y, Tian J, et al. Interlaminar failure behavior of GLARE laminates under short-beam three-point-bending load. Compos Part B Eng. 2016;97(May):361–7.

[16] Pahr DH, Rammerstorfer FG, Rosenkranz P, Humer K, Weber HW. A study of short-beam-shear and double-lap-shear specimens of glass fabric/epoxy composites. Compos Part B Eng. 2002;33(2):125–32.

[17] Chen Y, Wang Y, Wang H. Research progress on interlaminar failure behavior of fiber metal laminates. Adv Polym Technol. 2020:1–20.

[18] Bieniaś J, Jakubczak P, Droździel M, Surowska B. Interlaminar shear strength and failure analysis of aluminium-carbon laminates with a glass fiber interlayer after moisture absorption. Materials (Basel). 2020;13(13):1–14.

[19] Hinz S, Omoori T, Hojo M, Schulte K. Damage characterisation of fibre metal laminates under interlaminar shear load. Compos Part A Appl Sci Manuf. 2009;40(6–7):925–31.

[20] Bellini C, Di Cocco V, Sorrentino L. Interlaminar shear

strength study on CFRP/Al hybrid laminates with different properties. Frat ed Integrita Strutt. 2020;14(51):442–8.

[21] Bahari-Sambran F, Meuchelboeck J, Kazemi-Khasragh E, Eslami-Farsani R, Arbab Chirani S. The effect of surface modified nanoclay on the interfacial and mechanical properties of basalt fiber metal laminates. Thin-Walled Struct. 2019;144:106343.

[22] Liu J, Xue W. Unconstrained bending and springback behaviors of aluminum-polymer sandwich sheets. Int J Adv Manuf Technol. 2017;91(5–8):1517–29.

[23] Tsukada T, Minakuchi S, Takeda N. Identification of process-induced residual stress/strain distribution in thick thermoplastic composites based on in situ strain monitoring using optical fiber sensors. J Compos Mater. 2019;53(24):3445–58.

[24] Yanagimoto J, Ikeuchi K. Sheet forming process of carbon fiber reinforced plastics for lightweight parts. CIRP Ann. 2012;61(1):247–50.

[25] Hu Y, Zhang Y, Fu X, Hao G, Jiang W. Mechanical properties of Ti/CF/PMR polyimide fiber metal laminates with various layup configurations. Compos Struct. 2019;229(June):111408.

[26] Che L, Zhou Z, Fang G, Ma Y, Dong W, Zhang J. Cured shape prediction of fiber metal laminates considering interfacial interaction. Compos Struct. 2018;194(April):564–74.

[27] Li H, Xu Y, Hua X, Liu C, Tao J. Bending failure mechanism and flexural properties of GLARE laminates with different stacking sequences. Compos Struct. 2018;187:354–63.

[28] Ma Y, Ueda M, Yokozeki T, Sugahara T, Yang Y, Hamada H. A comparative study of the mechanical properties and failure behavior of carbon fiber/epoxy and carbon fiber/polyamide 6 unidirectional composites. Compos Struct. 2017;160:89–99.

[29] Dhaliwal GS, Newaz GM. Experimental and numerical investigation of flexural behavior of carbon fiber reinforced aluminum laminates. J Reinf Plast Compos. 2016;35(12):945–56.

Received 2022-01-18
Accepted 2022-05-30